RSC Advances

PAPER

View Article Online
View Journal | View Issue

Cite this: *RSC Adv.*, 2025, **15**, 36907

Manganese-based nanotheranostics synergizing photothermal-chemotherapy for liposarcoma treatment

Wenhua Zhan, *[ad] Shangting Du, [a] Tianyi Zhu, [a] Yingying Liu, [a] Lingyu Li, [a] Yueyang Gao, [b] Yijun Lu [c] and Wei Wang *[a]

Liposarcoma (LPS), the most common subtype of soft tissue sarcoma, presents significant therapeutic challenges due to its high heterogeneity, frequent recurrence, and adverse effects on conventional treatments. In this study, we developed multifunctional manganese-based nanotheranostics by integrating Mn_3O_4 nanoparticles (Mn_3O_4 NPs), doxorubicin (DOX), and photosensitizer IR-780, with surface modification using polydopamine (PDA). The manganese-DOX-IR-780 nanoparticles (MDI NPs) exhibited a uniform particle size distribution, excellent colloidal stability, biocompatibility, and pH-responsive drug release capability. Additionally, they achieved efficient photothermal heating, reaching temperatures of 70–80 °C, with a photothermal conversion efficiency (PCE) of 47.6%. Notably, the longitudinal relaxivity of MDI NPs ($r_1 = 1.827\ mM^{-1}\ s^{-1}$) was 10.02-fold higher than that of Mn_3O_4 NPs ($r_1 = 0.1824\ mM^{-1}\ s^{-1}$), demonstrating its potential as an efficient MRI contrast agent for real-time therapeutic monitoring, with favorable *in vivo* MRI imaging performance. *In vitro* experiments revealed that MDI NPs effectively inhibited LPS cell growth with a strong synergistic effect (combination index, CI = 0.17). *In vivo* studies showed that MDI NPs could accumulate at tumor sites and sustain drug release for over 72 hours. Under mild photothermal conditions (43–45 °C), MDI NPs achieved a remarkable tumor suppression rate of 94.3% and a cure rate of 75%. This study provides a novel, low-toxicity, and highly effective theranostic strategy to overcome the therapeutic challenges of LPS, with significant clinical translation potential.

Received 21st May 2025
Accepted 29th September 2025

DOI: 10.1039/d5ra03568f

rsc.li/rsc-advances

1 Introduction

Liposarcoma (LPS), representing approximately 20% of all soft tissue malignancies in adults, is the most common subtype of soft tissue sarcoma.[1] Pathologically, LPS is characterized by proliferating adipocytic tumor cells exhibiting varying degrees of differentiation and atypia.[2] According to the 2020 World Health Organization classification of soft tissue tumors, LPS is categorized into four distinct subtypes: well-differentiated (WDLS), dedifferentiated (DDLS), myxoid/round cell (MRCLS), and pleomorphic (PLS) – each demonstrating unique molecular profiles, aggressiveness, and treatment responsiveness.[3,4] While complete surgical resection (R0 resection) remains the only potentially curative approach, approximately 50% of cases fail to achieve optimal resection margins due to anatomical constraints and locally invasive tumor characteristics.[5,6] Chemotherapy, particularly doxorubicin (DOX)-based regimens, serves as the mainstay systemic treatment. DOX exerts its therapeutic effects by persistently (≥48 hours) intercalating tumor cell deoxyribonucleic acid (DNA) at both primary and metastatic sites.[7] However, its clinical utility is significantly limited by dose-dependent cardiotoxicity, drug resistance, and suboptimal therapeutic outcomes.[8] Notably, certain subtypes like DDLS and PLS demonstrate particularly poor responses to chemotherapy, underscoring the urgent need for novel combinatorial therapeutic strategies.[9,10]

Nanomedicine offers a promising solution to these therapeutic challenges. Leveraging the unique enhanced permeability and retention (EPR) effect in tumor tissues,[11] nanocarriers not only enable targeted drug delivery but also facilitate the integration of multiple treatment modalities for synergistic therapeutic optimization through distinct mechanisms.[12] Current research has documented various combination strategies for sarcoma treatment, including chemotherapy paired with targeted therapy, immunotherapy, or photothermal therapy (PTT).[13–15] The PTT-chemotherapy combination demonstrates particular advantages. PTT employs

[a]*Department of Radiation Oncology, General Hospital of Ningxia Medical University, Yinchuan, Ningxia Hui Autonomous Region, 750004, China. E-mail: zhanwhgood@163.com; wwycy2009146@163.com*

[b]*College of Clinical Medicine, Xi'an Medical University, Xi'an, Shaanxi, 710021, China*

[c]*School of Life Science and Technology, Xidian University, Xi'an, Shaanxi, 710126, China*

[d]*State Key Laboratory of Pathogenesis, Prevention and Treatment of High Incidence Diseases in Central Asia, Xinjiang Medical University, Urumqi, Xinjiang Uygur Autonomous Region, 830054, China*

photothermal agents to generate localized hyperthermia at target sites, inducing tumor cell death through irreversible membrane damage and protein denaturation. This approach offers notable benefits including rapid treatment completion (typically within minutes) and remarkable therapeutic efficacy.[16,17] However, standalone PTT often fails to eradicate diffuse lesions completely and may leave residual tumor margins untreated.[18] The strategic combination of PTT with chemotherapy creates a synergistic therapeutic approach that harnesses the complementary advantages of both modalities. The localized hyperthermia generated by PTT directly induces rapid tumor cell death through thermal ablation, providing immediate cytotoxic effects.[19] Concurrently, the thermally-induced enhancement of cell membrane permeability facilitates significantly improved intracellular uptake of chemotherapeutic agents while simultaneously mitigating drug resistance.[20] This dual-action strategy establishes a novel treatment paradigm for LPS that is simultaneously precise, potent, and low-toxicity.

The marked tumor heterogeneity in LPS leads to significant spatiotemporal heterogeneity in tumor cell responses to treatment.[21] Therefore, real-time monitoring during therapy and timely adjustment of treatment regimens based on therapeutic efficacy are particularly crucial. By integrating diagnostic and therapeutic functions into a single nanoplatform, precise monitoring of the treatment process can be achieved. Manganese-based nanomaterials demonstrate unique advantages in LPS theranostics due to their distinctive enzyme-like activities and magnetic resonance imaging (MRI) capabilities.[22,23] Particularly, MRI has been established as the preferred modality for clinical diagnosis and therapeutic evaluation of LPS owing to its exceptional soft tissue resolution.[24]

Polydopamine (PDA), a synthetic analogue of natural melanin, possesses unique structural features—its aromatic ring framework is rich in functional groups such as catechols, amines, and imines.[25,26] These characteristics enable PDA to form stable π–π interactions with planar aromatic molecules like DOX and IR-780, facilitating their hybrid assembly within the PDA matrix during its polymerization process. This mechanism is supported by the well-documented property of PDA to load drug molecules *via* π–π interactions, which has been widely utilized in drug delivery systems.[27,28] Furthermore, PDA exhibits zwitterionic properties. Under acidic conditions, its amino groups undergo protonation, conferring a positive charge, while under alkaline conditions, deprotonation of phenolic groups results in a negative charge.[29] This pH-dependent ionization influences the adsorption and release of charged drug molecules. Thus, the charge characteristics of PDA and the drug can be leveraged to design nanocarriers capable of tumor microenvironment-responsive drug release, promoting retention during circulation and triggered release in the acidic tumor milieu.[30] Notably, PDA polymerization occurs under simple and mild conditions, allowing for the *in situ* encapsulation of DOX and IR-780 as the PDA layer forms around the Mn_3O_4 NPs core.[31] This design leverages PDA's dual role as a protective barrier and drug reservoir, ensuring efficient co-delivery. Building upon this foundation, our study developed manganese-DOX-IR-780 nanoparticles (MDI NPs).[32] Utilizing MRI-visible Mn_3O_4 NPs as the core, core–shell structured MDI NPs were successfully constructed through spontaneous oxidative polymerization of dopamine under mild alkaline conditions, which simultaneously enabled efficient co-loading of the photosensitizer IR-780 and the chemotherapeutic drug DOX into the PDA matrix *via* π–π stacking interactions. The resulting MDI NPs exhibited uniform size distribution, excellent photothermal heating capability (reaching 70–80 °C within 5 minutes) with a photothermal conversion efficiency (PCE) of 47.6%, colloidal stability, and biocompatibility. Relaxivity measurements revealed that MDI NPs demonstrated a longitudinal relaxivity ($r_1 = 1.827\ mM^{-1}\ s^{-1}$), representing a 10.02-fold enhancement over Mn_3O_4 NPs ($r_1 = 0.1824\ mM^{-1}\ s^{-1}$), highlighting their significant potential as MRI contrast agents for real-time treatment monitoring. *In vitro* studies showed that MDI NPs effectively inhibited liposarcoma cell growth through combined photothermal-chemotherapy, with a combination index (CI) of 0.17. *In vivo* fluorescence imaging demonstrated efficient tumor accumulation and sustained drug release (>72 h). *In vivo* MRI detection revealed superior imaging performance. Under mild photothermal conditions (43–45 °C), the treatment achieved 94.3% tumor suppression and 75% cure rates, establishing a gentle, low-toxicity yet highly effective synergistic therapy. These findings provide both theoretical foundations and practical solutions for LPS treatment with real-time efficacy monitoring.

2 Materials and methods

2.1. Materials

DMEM high-glucose medium was purchased from Pricella Biotechnology Co., Ltd (Shanghai, China). Trypsin, fetal bovine serum (FBS), DOX, dimethyl sulfoxide (DMSO) and coumarin 6 were obtained from Aladdin (Shanghai, China). IR-780, Tween 80, manganese acetate, oleic acid, oleylamine, xylene, and cyclohexane were acquired from Sigma-Aldrich (Shanghai, China). The Cell Counting Kit-8 (CCK-8) and Calcein-AM/PI cell viability/cytotoxicity assay kits were procured from Beyotime Biotechnology Co., Ltd (Shanghai, China). Tris hydrochloride, Pluronic F-127, and PDA were sourced from Macklin Biochemical Co., Ltd (Shanghai, China). Cell lines, including the human liposarcoma cell line (SW-872), human embryonic kidney cell line (HEK-293), and human fetal lung fibroblast cell line (IMR-90), were purchased from Coweldgen Scientific Co., Ltd (Shanghai, China), with all lines originally derived from the American Type Culture Collection (ATCC). All experimental animals were supplied by Beijing HFKBio PLC (Beijing, China).

2.2. Preparation of MDI NPs

The synthesis of Mn_3O_4 NPs was performed according to the method reported by Yang *et al.*[32] Briefly, manganese acetate (1 mmol, 0.17 g), oleic acid (640 μL), and oleylamine (3.28 mL) were dissolved in 15 mL of xylene. The mixture was gradually heated to 90 °C and reacted for 10 min. Subsequently, 1 mL of deionized water was added, and the reaction was continued at

90 °C for 2.5 h. The product was then precipitated by adding 45 mL of anhydrous ethanol, followed by centrifugation. The obtained Mn_3O_4 NPs were dispersed in cyclohexane for further use. For MDI NPs preparation, 12 mg of IR-780 and 45 mg of Pluronic F-127 were dissolved in 1 mL of DMSO. This solution was slowly added dropwise to 9 mL of tris buffer containing 35 mg of Mn_3O_4 NPs under continuous magnetic stirring (Great Wall Science and Trade Co., Ltd, Zhengzhou, China). Subsequently, 4 mg of DOX was added with constant stirring. The mixture was stirred for an additional 20 min, followed by sonication at 150 W for 5 min using an ultrasonic homogenizer (Five Phase Instrument & Meter Co., Ltd, Shanghai, China) to ensure complete dissolution. Next, 10 mg of PDA was slowly added to the mixture with continuous stirring for 5 min. The final solution was protected from light and allowed to react under rotary conditions for 72 h. The product was then dialyzed to remove DMSO and other soluble impurities, yielding the manganese-DOX-IR-780 nanoparticles (MDI NPs).

2.3. Characterization and *in vitro* MRI imaging of MDI NPs

The morphology of Mn_3O_4 NPs and MDI NPs was examined using transmission electron microscopy (TEM; Thermo Fisher Scientific, Waltham, MA, USA) and scanning electron microscopy (SEM; Carl Zeiss AG, Oberkochen, Germany). Particle size and zeta potential was measured with a Malvern Zetasizer (Malvern Instruments Ltd, Worcestershire, UK). To evaluate colloidal stability, MDI NPs were dispersed in culture medium, phosphate-buffered saline (PBS), or serum, with hydrodynamic diameter monitored over time using the same instrument. Drug loading capacity (DLC) and encapsulation efficiency (EE) were quantified by high-performance liquid chromatography (HPLC) with the following calculations:

$$\mathrm{EE}(100\%) = \frac{M_{\text{drug input}} - M_{\text{drug remain}}}{M_{\text{drug input}}}$$

$$\mathrm{DLC}(100\%) = \frac{M_{\text{drug input}} - M_{\text{drug remain}}}{M_{\text{MDI NPs input}}}$$

To simulate the tumor microenvironment, the release behaviors of DOX and IR-780 from MDI NPs were investigated in PBS buffers at pH 5.5 and 7.4. The MDI NPs solution (1 mg mL^{-1}) was placed in a dialysis bag (MWCO 3500 Da) and immersed in PBS buffers at the respective pH values under continuous stirring at 150 rpm and 37 °C for 72 hours. The release of IR-780 was studied simultaneously under identical conditions, with 1% Tween 80 added to the external dialysis medium to enhance its dissolution. Samples of the dialysate were collected at predetermined time intervals, and the UV-Vis absorptions were measured at $\lambda = 480$ nm and $\lambda = 808$ nm using a UV-Vis spectrophotometer (T6, Persee, Shanghai, China) to determine the release of DOX and IR-780, respectively. After each sampling, an equal volume of fresh PBS buffer was replenished to maintain sink conditions.

A 0.5 T small-animal MRI scanner (Bruker, Billerica, Germany) was used to measure the relaxation times of Mn_3O_4 NPs and MDI NPs at varying concentrations and T_1-weighted MR images of MDI NPs at different concentrations. T_1 contrast properties were validated by constructing the scatterplot of the relaxation rate *vs.* relaxation time. The longitudinal relaxivity (r_1) was determined *via* linear regression of $1/T_1$ (s^{-1}) *versus* nanoparticle concentration (mM).

The T_1-weighted MRI properties were validated by measuring the relaxation times of Mn_3O_4 NPs and MDI NPs at different concentrations using a 0.5 T small-animal MRI scanner (Bruker, Billerica, Germany), along with relaxation-weighted images of MDI NPs at varying concentrations. A scatter plot of relaxation time *versus* relaxivity was generated, and the r_1 values were calculated through linear regression of $1/T_1$ (s^{-1}) against the concentrations (mM) of Mn_3O_4 NPs and MDI NPs. The conventional spin-echo acquisition sequence parameters were set as follows: repetition time = 400 ms, echo time = 18.2 ms, slice gap = 0.8 mm, slice width = 3 mm.

2.4. Photothermal conversion performance of MDI NPs

An 808 nm laser (BOT Optoelectronics Technology Co., Ltd, Xi'an, China) was used to irradiate the samples under different conditions, and temperature changes were monitored using an infrared thermal imaging camera (FLIR Systems, Inc., Wilsonville, Oregon, USA). Unless otherwise specified, all experiments were conducted with an MDI NPs concentration of 243 μg mL^{-1}. First, MDI NPs samples were irradiated with an 808 nm laser (BOT Optoelectronics Technology Co., Ltd, Xi'an, China) at a power density of 2 W cm^{-2}, while temperature was recorded every 20 s using the infrared thermal imaging camera (FLIR Systems, Inc., Wilsonville, Oregon, USA) until the temperature reached a maximum and stabilized. After removing the irradiation, the samples were allowed to cool before repeating the process to assess the photothermal stability of MDI NPs. Additionally, the PCE is a crucial parameter for evaluating the photothermal performance of molecules. Based on the cooling phase of MDI NPs, a curve of cooling time (t) *versus* the negative natural logarithm of the temperature drive ($-\ln\theta$) was obtained, and the PCE of MDI NPs was further calculated according to established literature methods (SI Methods 1).[33] Next, the photothermal stability of MDI NPs and its individual components (IR-780, PDA, Mn_3O_4 NPs, and DOX) at the same concentration (243 μg mL^{-1}) were evaluated under 2 W cm^{-2} irradiation for 5 min, with temperature recorded every 10 s. Subsequently, the photothermal conversion capability of MDI NPs was systematically evaluated under varying parameters: different power densities (0.5, 1, 1.5, and 2 W cm^{-2}), different concentrations (243, 81, 27, 9, and 3 μg mL^{-1}), and different dispersion media (serum, PBS, and culture medium). For all these tests, samples were irradiated for 5 min with temperature recorded at 10 s intervals. For *in vitro* testing, samples were overlaid with precisely measured fat and muscle tissue layers (1, 2, and 3 mm thickness) to simulate biological barriers. Additionally, *in vivo* photothermal conversion performance was examined in BALB/c mice by evaluating subcutaneous and

intramuscular temperature changes under identical irradiation conditions (5 min exposure with 10 s interval monitoring).

2.5. Cellular internalization assay of MDI NPs

To effectively visualize nanoparticle internalization, MDI NPs were fluorescently labeled using coumarin 6 (green fluorescence) and DOX (red fluorescence). SW-872 cells were seeded at a density of 2×10^4 cells per dish in confocal imaging dishes and incubated at 37 °C under 5% CO_2. After cell adhesion, fluorescently labeled MDI NPs were added to the culture medium for further incubation. At designated time points (1, 2, 4, and 6 hours), the dishes were removed, fixed with paraformaldehyde, and stained with DAPI for nuclear visualization. The intracellular localization of MDI NPs was observed using a laser scanning confocal microscope (Leica, Wetzlar, Germany), followed by quantitative fluorescence intensity analysis.

To investigate the cellular uptake mechanism, sodium azide (NaN_3), an inhibitor of active transport, was employed. SW-872 cells (2×10^4 cells) were seeded in 3.5 cm confocal dishes and cultured under standard conditions (37 °C, 5% CO_2). Following cell adhesion, the cultures were divided into two groups: the experimental group pretreated with 50 mmol L^{-1} NaN_3 to block active transport, and the untreated control group. Both groups were incubated with MDI NPs for 4 hours, then fixed with paraformaldehyde and stained with DAPI. Cellular fluorescence distribution was examined by confocal microscopy (Leica, Wetzlar, Germany), with quantitative fluorescence intensity analysis performed using Image J software.

2.6. *In vitro* cytotoxicity evaluation of MDI NPs

The cytotoxic effects of MDI NPs and their primary components were assessed using the CCK-8 assay across three cell lines: two normal cell lines (HEK-293 and IMR-90) and the human LPS cell line SW-872. Cells in the logarithmic growth phase were trypsinized to prepare single-cell suspensions, which were then seeded in 96-well plates at a density of 8×10^4 cells per well. Following cell adhesion, test samples were added to the wells in concentration gradients, with each concentration tested in triplicate wells during incubation at 37 °C under a 5% CO_2 atmosphere. The concentration ranges for each test compound were determined based on their mass ratios in MDI NPs and corresponding drug loading capacities. When control wells reached approximately 80% confluence, the culture medium was replaced with phenol red-free medium containing CCK-8 reagent. After an additional 1.5-hours incubation period, absorbance measurements were obtained at 450 nm using a microplate reader (Tecan Group Ltd, Männedorf, Switzerland) to calculate cell viability percentages.

The combined therapeutic efficacy of MDI NPs on SW-872 cells was systematically evaluated through CCK-8 assay, colony formation test, and live/dead cell staining. SW-872 cells in good growth condition were seeded in 96-well plates at a density of 1.2×10^5 cells per well and incubated overnight at 37 °C with 5% CO_2. The cells were then treated with various concentrations of MDI NPs (ranging from 4 μg mL^{-1} to 16 μg mL^{-1}, with two experimental groups at the 16 μg mL^{-1} concentration). Following overnight incubation, the plates were subjected to 808 nm laser irradiation (1 W cm^{-2}) while monitoring temperature with an infrared thermal imager, maintaining the temperature between 43-45 °C for a total irradiation duration of 4 minutes. One 16 μg mL^{-1} group served as a non-irradiated control. After an additional 4-hours incubation, cell viability was determined using the same methodology. The half-maximal inhibitory concentrations (IC50) were calculated from dose–response curves for IR-780 with laser, DOX, and MDI NPs with laser treatments. The CI of MDI NPs was subsequently determined using the Chou-Talalay method (SI Methods 2).[34] Colony formation assays were performed to assess the proliferative capacity of SW-872 cells under different treatment conditions. Pre-cultured cells were trypsinized and resuspended in 1.5 mL centrifuge tubes, then treated with IR-780 (3 μg mL^{-1}), DOX (1 μg mL^{-1}), IR-780 + DOX combination, or MDI NPs. Each well received 808 nm laser irradiation (1 W cm^{-2}) for 1 minute while maintaining the temperature at 43–45 °C, after which cells were transferred to 6 cm culture dishes. Colonies containing more than 50 cells were fixed, stained, and quantified using Image J software. For live/dead cell staining, cells were seeded in 24-well plates at 1×10^5 cells per well and allowed to reach 70% confluence before treatment. After 24 hours of incubation, cells were stained using a live/dead cell staining kit (AM : PI : buffer = 1 : 1 : 1000 ratio), protected from light for 30 minutes, and then examined under an inverted fluorescence microscope (Leica, Wetzlar, Germany).

2.7. Biocompatibility assessment of MDI NPs *via* hemolysis assay

The hemolytic potential of MDI NPs and their individual components was evaluated to assess biocompatibility. Experimental groups included MDI NPs, Mn_3O_4 NPs, IR-780, and DOX, with 0.1% Triton X-100 serving as the positive control. A 6% suspension of sheep red blood cells (RBCs) was diluted to 2% using 0.9% NaCl. For testing, 1 mL of test solution (containing 5% sample and 95% 2% RBCs suspension) was prepared in 1.5 mL centrifuge tubes. Initial photographs were taken against a white background before incubation. The samples were then incubated in a 37 °C water bath for 2 hours. Following incubation, the tubes were centrifuged at 10 000 rpm for 2 minutes, and post-centrifugation images were captured under identical background conditions. Hemoglobin release was quantified by measuring absorbance at 405 nm using a microplate reader, and the hemolysis percentage was calculated accordingly.

The approximate lethal dose ranges of various compounds were determined through acute toxicity testing. Ten BALB/c mice per group (equal gender distribution) were utilized to minimize sex-related variability. Following an overnight fasting period, test compounds were administered *via* tail vein injection at specified doses: MDI NPs (135 mg kg^{-1}), Mn_3O_4 NPs (45 mg kg^{-1}), IR-780 (15 mg kg^{-1}), and DOX (5 mg kg^{-1}). Food and water were restored 2 hours post-injection. Continuous monitoring of vital signs was conducted for 14 days with mortality rates recorded. From each group, three randomly

selected mice underwent orbital venous blood collection for comprehensive analysis, including standard biochemical parameters and inflammatory markers (TNF-α and IL-6). Following euthanasia, major organs (heart, liver, spleen, lungs, and kidneys) were harvested for histopathological examination *via* hematoxylin and eosin (H&E) staining. All experimental procedures strictly adhered to animal welfare guidelines and were performed in accordance with protocols approved by Xi'an Medical University's Institutional Animal Care and Use Committee (Approval No.: XYLS-2022188).

2.8. Establishment of LPS-induced subcutaneous tumor xenograft model

Following a one-week acclimatization period under specific pathogen-free (SPF) conditions, 4-weeks-old nude mice received subcutaneous injections of 100 μL SW-872 cell suspensions (5×10^5 cells per mL). Post-inoculation, all animals were maintained in SPF environments until tumors reached appropriate volumes ($\sim$30 mm^3; about 1 week after inoculation) for subsequent *in vivo* antitumor efficacy evaluation.

2.9. *In vivo* biodistribution, targeted delivery and MRI evaluation of MDI NPs

Tumor-bearing mice maintained under SPF conditions were selected for biodistribution studies when tumors reached appropriate volumes ($\sim$30 mm^3; about 1 week after inoculation). Mice with comparable tumor sizes were randomly divided into two groups ($n = 3$). The experimental group received 200 μL MDI NPs *via* tail vein injection, while the control group was administered free IR-780 through intravenous delivery. Post-injection, mice were subjected to *in vivo* fluorescence imaging using a small animal imaging system (Vieworks Co., Ltd, Gyeonggi-do, South Korea) under isoflurane anesthesia. Fluorescence images were acquired at predetermined time intervals (1, 4, 6, 8, 12, 24, 48, and 72 hours). Following 72-hours observation, euthanized mice underwent organ collection (heart, liver, spleen, lungs, kidneys, and tumors) after *in vivo* fluorescence analysis under consistent imaging parameters to determine the biological distribution profile of MDI NPs across various tissues. Next, we conducted comprehensive *in vivo* MRI studies to assess the MRI performance of MDI NPs. Tumor-bearing mice were intravenously administered 200 μL of MDI NPs (experimental group) or an equivalent volume of saline (control group). T_1-weighted MRI images were acquired at various time points using a 0.5 T small-animal MRI scanner (Bruker, Billerica, Germany).

2.10. *In vivo* antitumor efficacy of MDI NPs

Twenty tumor-bearing mice maintained under SPF conditions were randomly allocated into five treatment groups when tumors reached appropriate volumes ($\sim$30 mm^3; about 1 week after inoculation). The experimental groups received 200 μL injections of either DOX (0.3 mg kg^{-1}), IR-780 (0.9 mg kg^{-1}), IR-780 + DOX combination, or MDI NPs (8.1 mg kg^{-1}), while the control group was administered an equivalent volume of physiological saline. Treatments were administered three times weekly. On the day following each injection, tumors were irradiated for 3 minutes using an 808 nm laser system (1 W cm^{-2}) with the probe fixed 15 cm above the target area, maintaining temperatures between 43–45 °C under isoflurane anesthesia. Tumor dimensions and body weights were monitored throughout the 22-days treatment period. Following euthanasia, excised tumors were measured and weighed for final evaluation.

2.11. Statistical analysis

All experimental data were analyzed using GraphPad Prism 10.0 software. Quantitative results are presented as mean ± standard deviation (Mean ± SD). For comparisons between two groups, independent samples *t*-test was employed for normally distributed data, while nonparametric tests were applied for non-normally distributed data. One-way analysis of variance (ANOVA) was utilized for multiple group comparisons. Statistical significance was defined as $P < 0.05$.

3 Results

3.1. Characterization and *in vitro* MRI performance of MDI NPs

MDI NPs were synthesized according to Scheme 1 and subsequently characterized. The TEM results show that the Mn_3O_4 NPs are spherical, well-dispersed, and approximately 10 nm in size (Fig. S1), while the MDI NPs also exhibit a uniform spherical morphology with good dispersion and an average diameter of 94.5 ± 4.1 nm (Fig. 1A). The SEM observations (Fig. S2) further support the spherical and monodisperse nature of both nanoparticle types, confirming the consistency between the TEM and SEM morphological data. Moreover, high-resolution TEM imaging (Fig. 1D) clearly reveals the high-density solid spherical structure of the MDI NPs, indicating that the PDA effectively integrates the initially dispersed Mn_3O_4 NPs into a compact core. These results clearly show that the small-sized Mn_3O_4 NPs are tightly and orderly arranged to form a well-defined core structure, which is completely encapsulated within a smooth and continuous PDA shell, collectively forming monodisperse nanoparticles with a core–shell architecture. Dynamic light scattering measurements demonstrated a slightly larger hydrodynamic diameter of 105.2 ± 1.1 nm (Fig. 1E), attributable to the hydration layer surrounding the nanoparticles. Zeta potential measurements confirmed moderate surface negative charges (−30 ± 4.5 mV, Fig. 1F). Stability assessments conducted in PBS, culture medium, and serum (Fig. 1H–J) showed less than 10% variation in particle size across all media. The encapsulation efficiencies for DOX and IR-780 were determined to be 86.9 ± 3.6% and 93.1 ± 4.4%, respectively, with corresponding drug loading capacities of 3.7 ± 1.8% and 11.1 ± 1.2%. These comprehensive characterizations validate MDI NPs as a stable multifunctional nanoplatform, establishing a solid foundation for subsequent *in vitro* and *in vivo* antitumor investigations.

The release profiles of DOX and IR-780 from MDI NPs were evaluated in PBS buffers at pH 5.5 and 7.4 to simulate their

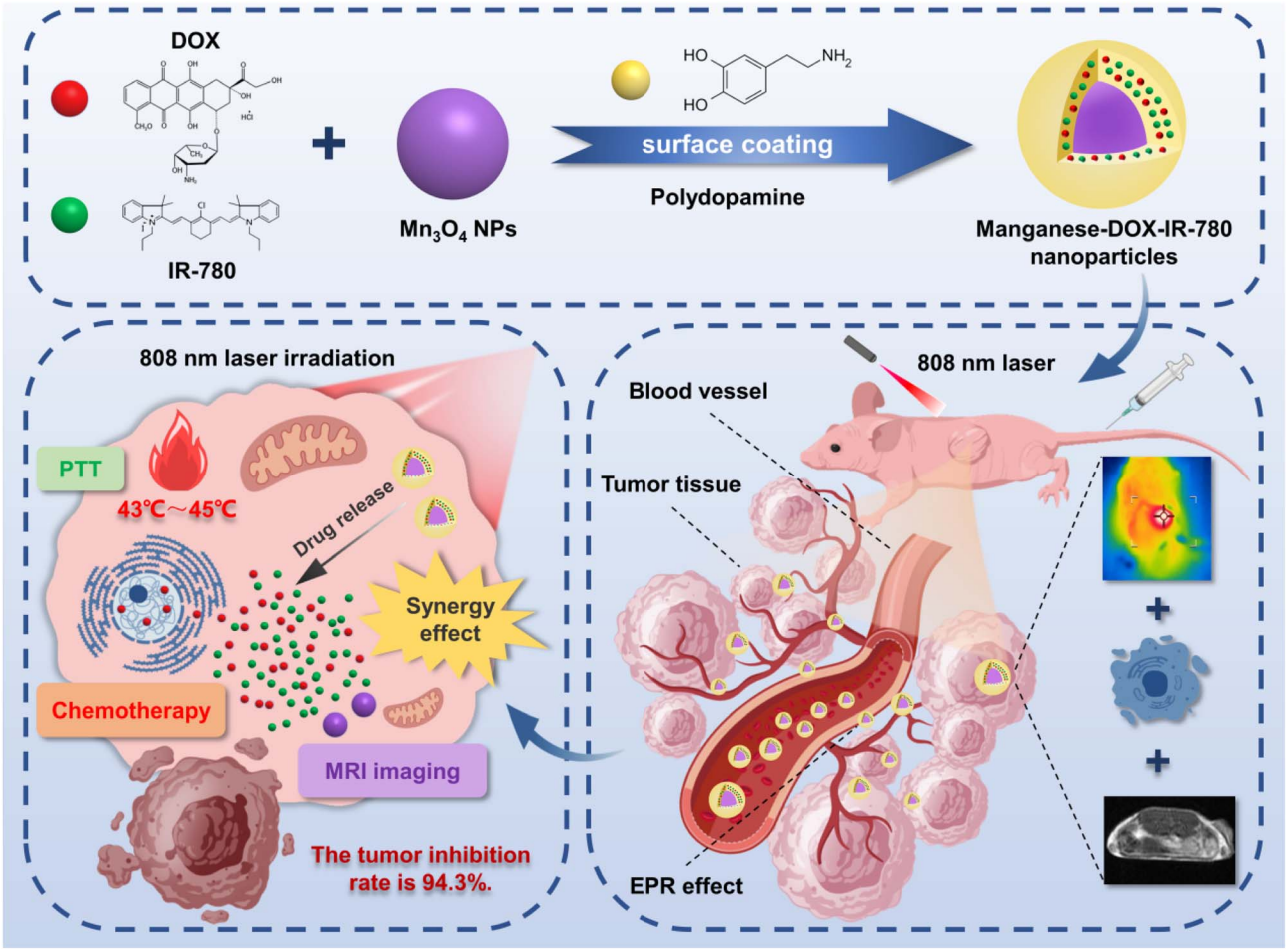

Scheme 1 Preparation of MDI NPs for photothermal-chemo synergistic therapy and MRI imaging.

release behavior under physiological and tumor microenvironment-mimicking conditions. As shown in Fig. S3, both drugs exhibited similar release trends. At pH 7.4, the PDA shell formed a loose protective layer, leading to sustained and limited drug release: the cumulative release rates of DOX and IR-780 at 24 h were 19.9% and 9.9%, respectively, which only increased to 22.4% and 11.3% at 72 h, demonstrating high stability under neutral pH. In contrast, at pH 5.5, the PDA layer underwent dissociation, resulting in rapid drug release: within 24 h, the release of DOX reached 97.9%, while that of IR-780 was 71.7%. By 72 h, DOX release was nearly complete (99.5%), whereas IR-780 showed slower release kinetics and a lower cumulative amount (72.3%) due to its higher hydrophobicity. These results confirm the pronounced pH-responsive release behavior of MDI NPs, enabling efficient drug release in the acidic tumor microenvironment and highlighting their potential for *in vivo* targeted therapy.

As manganese-based MRI contrast agents,[35] both Mn_3O_4 NPs and MDI NPs were evaluated for their relaxivity rates. Linear regression analysis of $1/T_1$ (s^{-1}) *versus* nanoparticle concentration (mM) revealed distinct longitudinal relaxivity (r_1) values: 0.1824 mM^{-1} s^{-1} for Mn_3O_4 NPs and 1.827 mM^{-1} s^{-1} for MDI NPs (Fig. 1B and C). Subsequent *in vitro* MRI evaluation demonstrated concentration-dependent signal enhancement for MDI NPs (Fig. 1G), with progressively intensified contrast corresponding to increasing nanoparticle concentrations. These findings not only correlate with the superior relaxivity characteristics of MDI NPs, but also substantiate their potential advantages as MRI contrast agents for real-time monitoring of LPS treatment efficacy.

3.2. Photothermal conversion performance of MDI NPs

A comprehensive evaluation of MDI NPs' photothermal properties was conducted. Photothermal stability tests demonstrated that MDI NPs could reach a maximum temperature of 70–80 °C with consistent heating performance, showing negligible reduction in peak temperature across three consecutive irradiation/cooling cycles (Fig. 2A), confirming excellent photothermal cycling stability. The PCE of MDI NPs, calculated from the natural cooling data of the first cycle, reached 47.6% (Fig. S4), demonstrating their high photothermal conversion capability. Comparative analysis of MDI NPs and their individual components (Fig. 2B) revealed IR-780 as the primary heat-generating moiety, with PDA contributing supplementary photothermal conversion capability, consistent with literature reports.[36] The synergistic combination of these components in

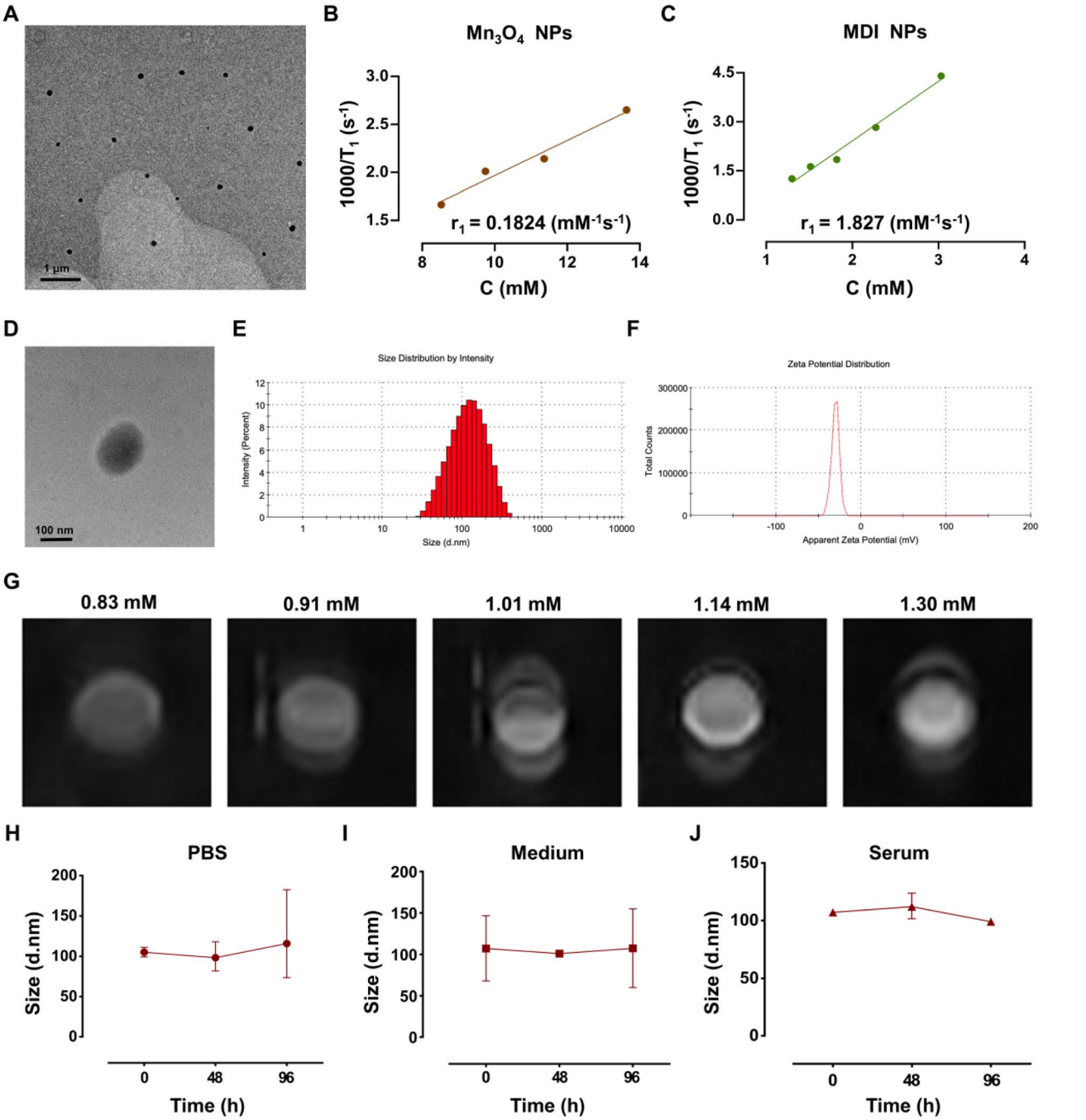

Fig. 1 Characterization and *in vitro* MRI performance of MDI NPs: (A) TEM image of MDI NPs (scale bar: 1 μm). (B) MRI relaxivity rates of Mn_3O_4 NPs. (C) MRI relaxivity rates of MDI NPs. (D) High-resolution TEM image of MDI NPs (scale bar: 100 nm). (E) Hydrodynamic size distribution of MDI NPs. (F) Zeta potential of MDI NPs. (G) Concentration-dependent MRI signal intensity of MDI NPs. (H–J) Size stability profiles of MDI NPs in PBS, culture medium, and serum, respectively. All data are presented as mean ± SD ($n = 3$).

MDI NPs resulted in the most rapid temperature elevation, demonstrating superior photothermal conversion capability. Power- and concentration-dependent studies (Fig. 2C and E) established a positive correlation between these parameters and MDI NPs' temperature elevation. Notably, MDI NPs maintained robust heating performance across various dispersion media (serum, PBS, and culture medium, Fig. 2D), ensuring compatibility with cellular experiments. Tissue penetration studies (Fig. 2F and G) confirmed effective heat generation through both adipose and muscle tissue barriers. Furthermore, *in vivo* assessments following subcutaneous and intramuscular administration (Fig. 2H and I) demonstrated significant temperature increases sufficient for practical photothermal therapy applications.

3.3. Cellular internalization evaluation of MDI NPs

The cellular uptake behavior of SW-872 cells was investigated using coumarin 6-loaded MDI NPs as fluorescent probes.

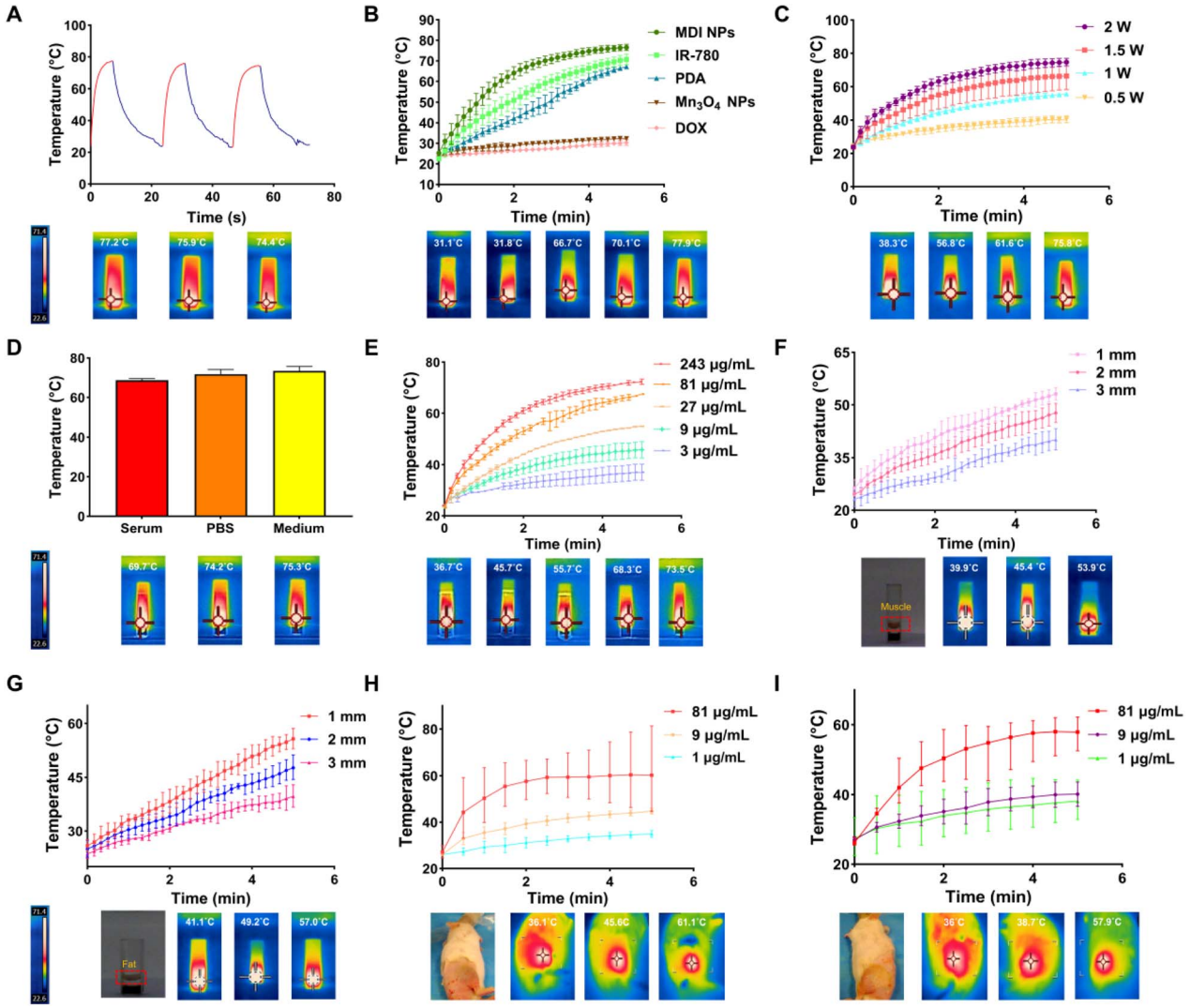

Fig. 2 Photothermal conversion performance of MDI NPs: (A) temperature variation curves of MDI NPs under three irradiation/cooling cycles; (B) temperature rise curves of MDI NPs and their components; (C) temperature rise curves of MDI NPs under different irradiation powers; (D) temperature rise curves of MDI NPs in different media; (E) temperature rise curves of MDI NPs at different concentrations; (F) temperature rise curves of MDI NPs under the coverage of muscle tissues of different thicknesses; (G) temperature rise curves of MDI NPs under adipose tissue coverage of different thicknesses; (H) temperature rise curves of subcutaneous injection of MDI NPs; (I) temperature rise curves of intramuscular injection of MDI NPs. Except for (C), the laser power of the remaining groups is set at 2 W cm^{-2}. The data are reported as mean ± SD ($n = 3$).

Fluorescence imaging revealed distinct cytoplasmic localization of both coumarin 6 (green) and DOX (red) signals within 1 hour of incubation (Fig. 3A and B). Time-dependent analysis demonstrated progressive intensification of these fluorescent signals in the cytoplasmic compartment. Notably, DOX exhibited nuclear accumulation due to its strong DNA-binding affinity, as evidenced by the increasing DOX/DAPI fluorescence ratio in nuclear regions after 6 hours (Fig. 3C). These observations confirm efficient cellular internalization of MDI NPs and subsequent payload delivery. Mechanistic studies employing sodium azide (NaN_3), an active transport inhibitor, demonstrated significantly reduced cellular fluorescence in pretreated cells compared to controls (Fig. 3D and E). Both microscopic imaging and quantitative fluorescence intensity analyses substantiate active transport as the predominant cellular entry mechanism for MDI NPs.

3.4. *In vitro* cytotoxicity evaluation of MDI NPs

The study employed two normal cell lines (HEK-293 and IMR-90) and one human LPS cell line (SW-872) to assess the cytotoxic effects of MDI NPs. As shown in Fig. 4A–C, Mn_3O_4 NPs and IR-780 exhibited negligible cytotoxicity across all cell lines, while both DOX and MDI NPs demonstrated concentration-dependent toxicity profiles. Notably, MDI NPs displayed comparable tumor suppression efficacy to free DOX, confirming successful chemotherapeutic agent delivery. Photothermal cytotoxicity assessment (Fig. 4D) revealed distinct response patterns under 808 nm laser irradiation (1 W cm^{-2}). MDI NPs showed pronounced concentration-dependent cytotoxicity, with cell viability decreasing to approximately 7% at the highest concentration (16 μg mL^{-1}). In contrast, without laser exposure, SW-872 cells maintained about 60% viability even at maximum

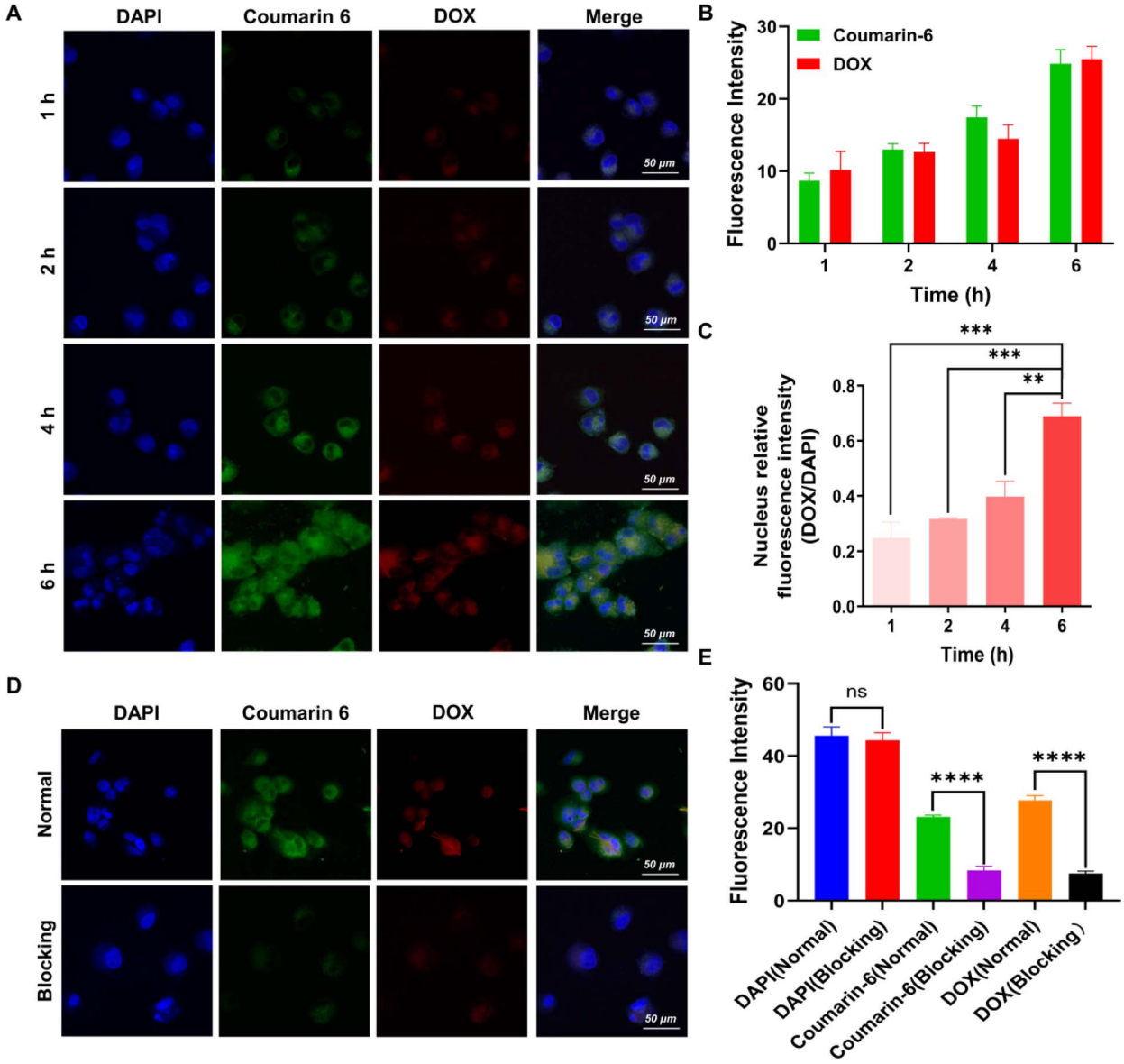

Fig. 3 Cellular internalization assessment of MDI NPs: (A) fluorescence micrographs of SW-872 cells following incubation with fluorescently labeled MDI NPs for 1, 2, 4, and 6 hours. (B) Quantitative analysis of fluorescence signals in cellular compartments. (C) Comparative nuclear fluorescence intensity ratios of DOX/DAPI. (D) Fluorescence visualization of MDI NPs internalization with or without NaN_3 pretreatment. (E) Statistical comparison of fluorescence signals between NaN_3-treated and control groups. Scale bars: 50 μm. Error bars represent standard deviation of the mean. *p < 0.05, **p < 0.01, ***p < 0.001, ****p < 0.0001. ns: not significant.

MDI NPs concentration. These findings collectively demonstrate the enhanced tumor cell inhibition achieved through combined MDI NPs and laser treatment. Colony formation assays revealed distinct proliferative capacities of SW-872 cells under various treatments (Fig. 4E). Control groups exhibited the highest cell density, while DOX and IR-780 + laser treatments showed significantly reduced colony numbers. The DOX + IR-780 + laser combination demonstrated greater suppression, with MDI NPs + laser treatment achieving the most pronounced anti-proliferative effect. Quantitative analysis using Image J software (Fig. 4F) confirmed these visual observations. Further validation through live/dead cell staining (Fig. 4G) identified MDI NPs-treated groups with the lowest cell viability. Dose–response curve analysis (Fig. S5) yielded IC50 values for IR-780 + Laser, DOX, and MDI NPs + Laser (Table S1), with the MDI NPs combination showing a CI value of 0.17. According to established criteria, CI values below 1.0 indicate synergistic effects, with values <0.8 representing significant synergy.[37] These comprehensive results demonstrate MDI NPs' ability to effectively integrate photothermal therapy and chemotherapy, exhibiting superior synergistic inhibition at the cellular level.

3.5. Biocompatibility assessment of MDI NPs

To evaluate the potential of MDI NPs for *in vivo* therapeutic applications, their biocompatibility and acute toxicity were

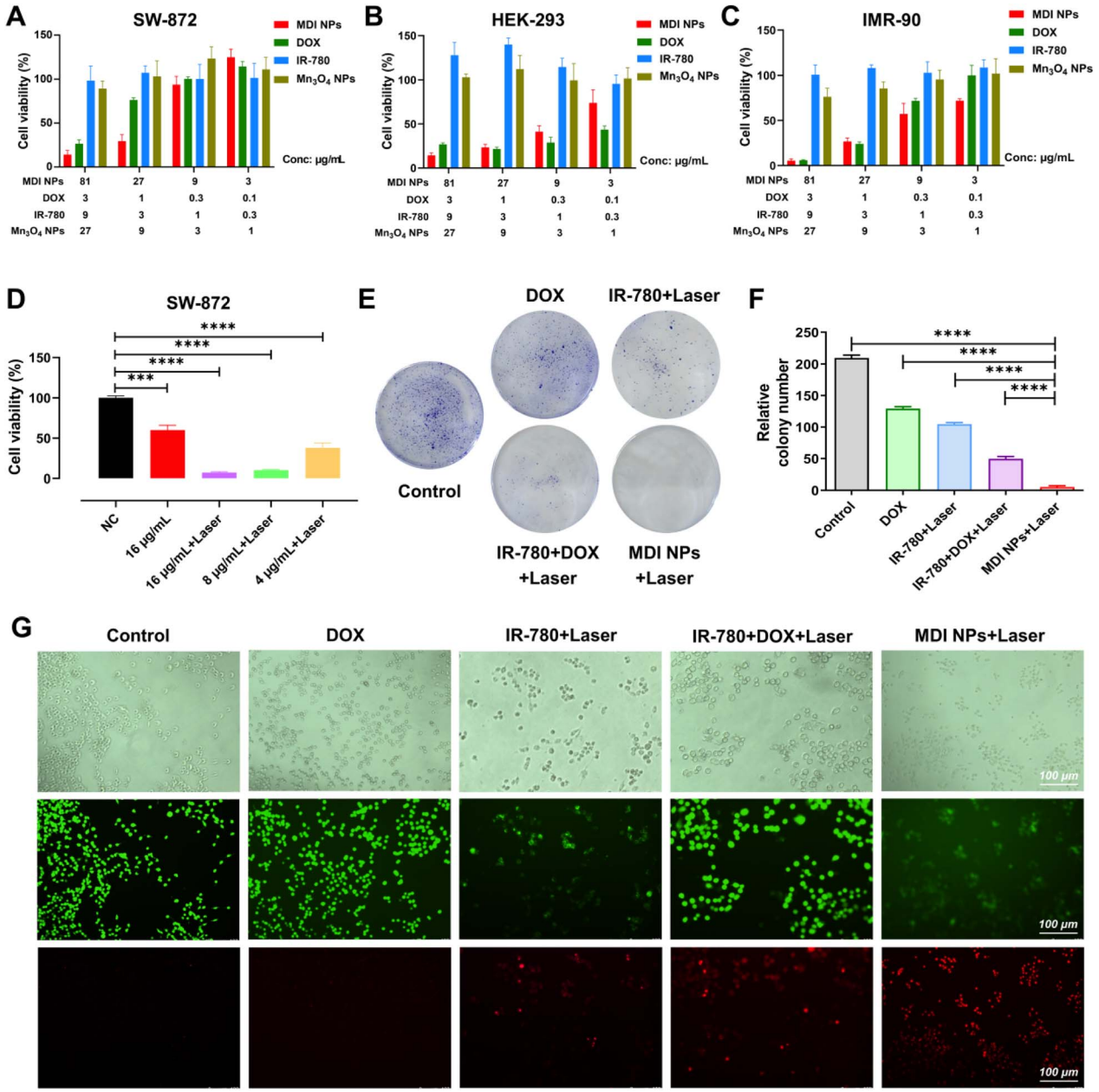

Fig. 4 *In vitro* toxicity evaluation of MDI NPs: (A–C) cytotoxicity test results of MDI NPs in SW-872, HEK-293, and IMR-90 cell lines; (D) cell viability of SW-872 cells treated with MDI NPs under 808 nm laser irradiation; (E) colony formation assay results of SW-872 cells after different treatments; (F) quantitative data of colony formation in SW-872 cells post-treatment; (G) fluorescence micrographs of live/dead cell staining in treated SW-872 cells. Scale bar, 100 μm. Error bars represent standard deviation of the mean. *$p < 0.05$, **$p < 0.01$, ***$p < 0.001$, ****$p < 0.0001$.

systematically investigated. As shown in Fig. 5A, the hemolysis rates of MDI NPs, as well as those of IR-780, Mn_3O_4 NPs, and DOX, were all below 5%, indicating no significant red blood cell lysis and confirming their safety for intravenous administration. Healthy BALB/c mice were divided into five groups (saline, MDI NPs, IR-780, Mn_3O_4 NPs, and DOX) to assess the acute toxicity of MDI NPs and their individual components. General health status, body weight, and mortality were monitored over a 14-days observation period. Fig. 5B and C demonstrate that none of the groups exhibited adverse effects such as convulsions, loss of appetite, significant weight loss, or mortality. Furthermore, the survival rate of all three biological replicates in each treatment group was 100%, with no variability in the data within or between groups. To further evaluate potential pathological effects on immune function, physiology, and major organs, mice were euthanized after 14 days. Heart, liver, kidney, and lung tissues, along with serum samples, were collected for histopathological analysis and biochemical inflammatory marker assessment. H&E staining revealed no notable pathological changes in major organs (Fig. 5D). Additionally, serum levels of TNF-α, IL-6, and liver/kidney function markers remained within normal ranges (Fig. S6). In summary,

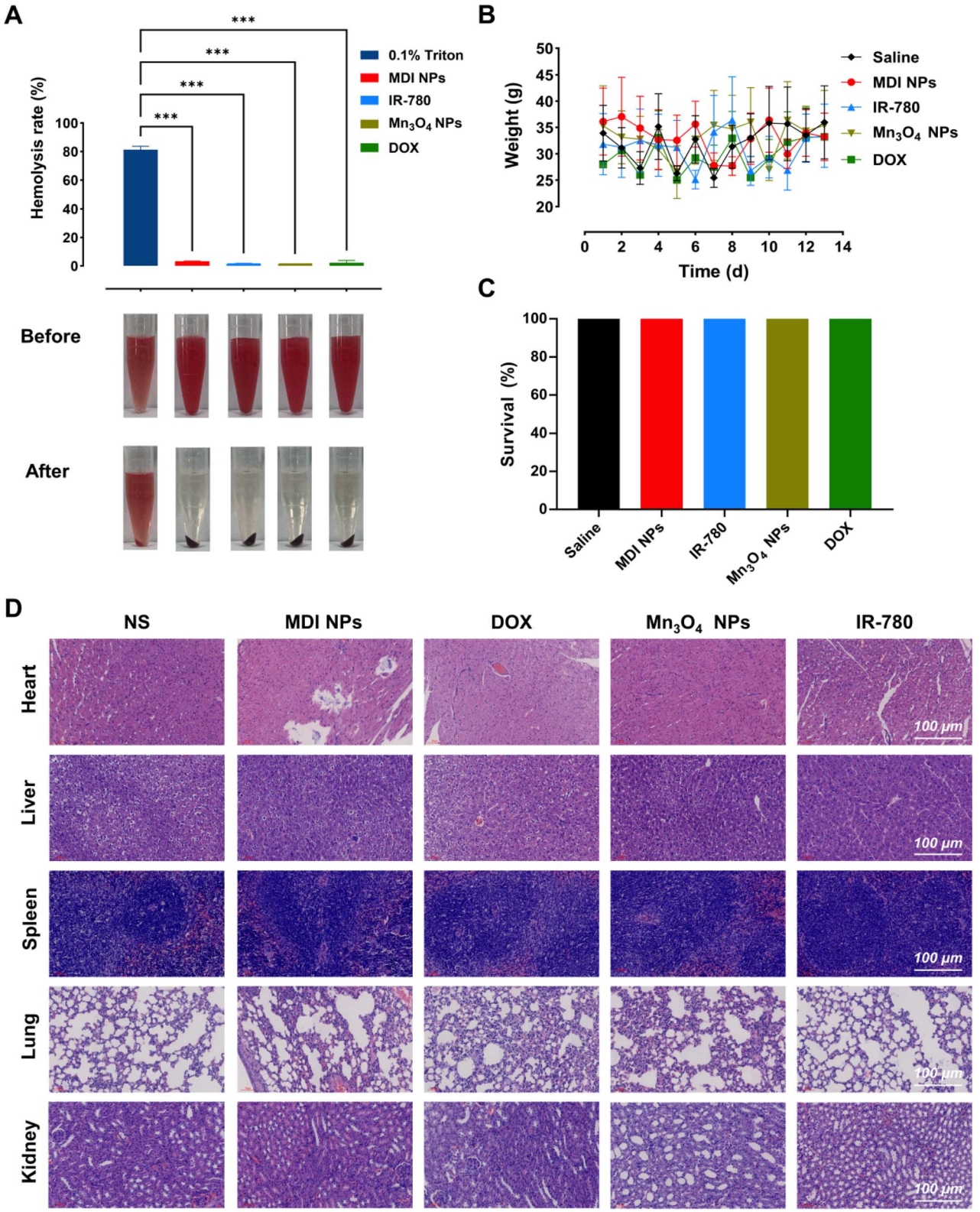

Fig. 5 Biocompatibility evaluation of MDI NPs: (A) hemocompatibility assessment of MDI NPs and their key components; (B) body weight changes in mice following treatment with MDI NPs and their components; (C) survival rates of mice after administration of MDI NPs and constituent materials; (D) H&E-stained sections of heart, liver, spleen, lungs, and kidneys from treated mice. Scale bar: 100 μm. Error bars represent mean ± SD. *$p < 0.05$, **$p < 0.01$, ***$p < 0.001$, ****$p < 0.0001$.

MDI NPs exhibit excellent biocompatibility, supporting their safe use for subsequent *in vivo* imaging and antitumor therapy studies.

3.6. *In vivo* distribution, targeted delivery and MRI evaluation of MDI NPs

The biodistribution of MDI NPs was investigated using a subcutaneous mouse model. Experimental mice received MDI NPs *via* tail vein injection, while control mice were administered an equivalent dose of saline. Fluorescence imaging was performed over 72 hours using an IVIS system. As shown in Fig. 6A, the experimental group exhibited distinct fluorescence signals at tumor sites, with progressive accumulation peaking at 24 hours before gradually declining, maintaining detectable signals beyond 72 hours. This demonstrates MDI NPs' ability to prolong systemic circulation and sustain drug release. Fig. 6B presents a quantitative analysis of fluorescence intensity, confirming the temporal pattern observed in imaging results, with statistically significant differences from the control group. After the *in vivo* imaging was completed, the mice were euthanized. The heart, liver, spleen, lungs, kidneys and tumors were collected, and the fluorescence signals of each organ were detected under the same conditions using the IVIS imaging system. Fig. 6C reveals a complete absence of fluorescence in control organs, while experimental mice showed predominant tumor accumulation. Quantitative measurements in Fig. 6D confirm targeted delivery, with fluorescence signals primarily localized in tumors ($p < 0.05$) and minimal accumulation in the liver, lungs, and kidneys (no statistical significance). This establishes MDI NPs' tumor-specific targeting capability as the foundation for their superior antitumor efficacy. Fig. 6E presents real-time MRI imaging results of mice over a 72-hours period. The saline control group showed no significant high-intensity signal in the tumor region. In contrast, the MDI NPs

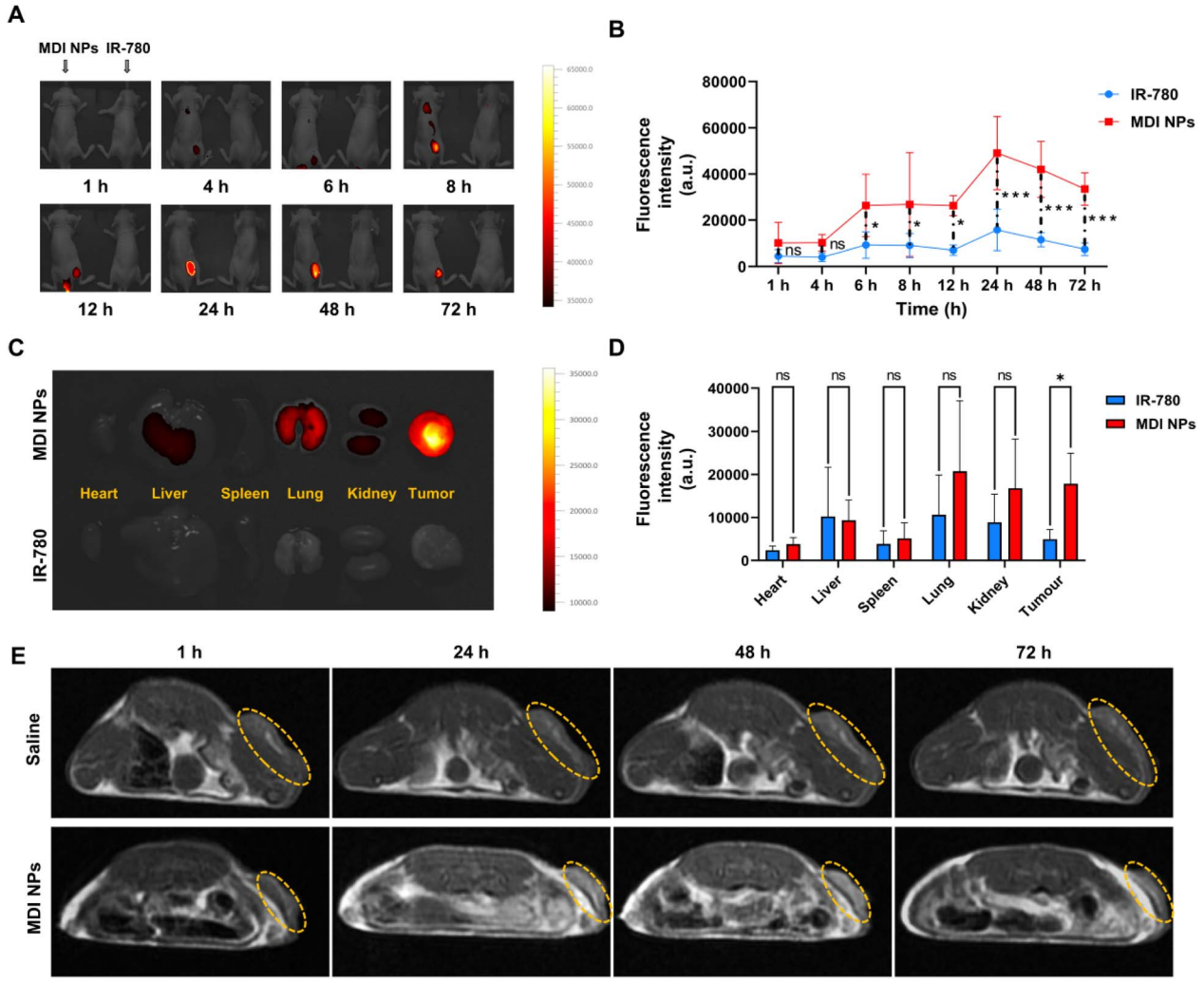

Fig. 6 *In vivo* biodistribution and targeting efficiency of MDI NPs: (A) real-time fluorescence imaging of MDI NPs distribution in mice over 72 hours; (B) quantitative analysis of fluorescence intensity at tumor sites; (C) fluorescence images of major organs and tumor tissues; (D) quantitative measurement of fluorescence signals in excised organs and tumors; (E) real-time MRI imaging of mice over 72 hours. The areas marked by the yellow dashed line are the tumor tissue regions. Error bars represent mean ± SD. *$p < 0.05$, **$p < 0.01$, ***$p < 0.001$, ****$p < 0.0001$, ns: not significant.

group demonstrated excellent T_1-weighted contrast enhancement, with the brightest tumor signal intensity observed at 24 hours post-injection, providing clear visualization of tumor margins and internal structures. The signal intensity gradually decreased thereafter but remained detectable for over 72 hours. These MRI findings are consistent with our fluorescence imaging results, demonstrating the outstanding MRI diagnostic potential of MDI NPs and establishing a solid foundation for their theranostic applications.

3.7. *In vivo* antitumor efficacy of MDI NPs

To evaluate the antitumor performance of MDI NPs *in vivo*, tumor-bearing mice were divided into treatment groups and monitored for 22 days, with tumor size and body weight regularly recorded. Photothermal therapy was administered using 808 nm laser irradiation (3 min, 1 W cm^{-2}), maintaining temperatures between 43–45 °C. Treatment commenced when subcutaneous tumors reached approximately 30 mm^3 (~1 week post-implantation). Fig. 7A displays representative tumor images, demonstrating superior therapeutic outcomes in the MDI NPs treatment group compared to the DOX, IR-780 + laser, and DOX + IR-780 + laser groups. Tumor growth curves were plotted based on volume measurements at different time points. As shown in Fig. 7B, within the first 12 days of intervention, all groups showed relatively slow tumor growth due to this early intervention and the small starting tumor size, with no significant differences between treatment arms at this stage. Importantly, in the later phase (tumors >100 mm^3), only the MDI NPs + laser combination demonstrated superior efficacy, achieving complete tumor regression, while other treatments showed limited suppression. Overall, the saline control group exhibited the most aggressive tumor progression, followed by the DOX group. While IR-780 + laser and DOX + IR-780 + laser treatments showed moderate tumor growth suppression, the MDI NPs + laser group achieved remarkable inhibition (94.3% suppression rate) with a 75% complete remission rate. These results confirm that MDI NPs combined with laser irradiation offer a highly effective and safe synergistic therapy *in vivo*.

4 Discussion

LPS presents significant clinical challenges due to its marked tumor heterogeneity and high recurrence rates. Current standard treatments remain dominated by surgical resection and chemotherapy. However, the invasive nature of surgery, coupled with the systemic toxicity and inconsistent short-term efficacy of chemotherapeutic agents, substantially limits their therapeutic outcomes in LPS patients. In contrast, nanomedicine platforms offer transformative potential by simultaneously enhancing drug targeting to improve therapeutic efficacy while reducing adverse effects. Their multifunctional design enables synergistic combination therapies with optimized safety profiles, along with real-time treatment monitoring capabilities – addressing critical limitations of conventional approaches.

This study successfully constructed MDI NPs with a stable core–shell structure by employing Mn_3O_4 NPs as an MRI-functional core, modifying the surface through PDA coating, and co-encapsulating both the photosensitizer IR-780 and the chemotherapeutic drug DOX *via* π–π stacking interactions. The synthesized MDI NPs exhibited a dense spherical core–shell structure with an optimal particle size of approximately 100 nm, along with excellent dispersibility and colloidal stability, which

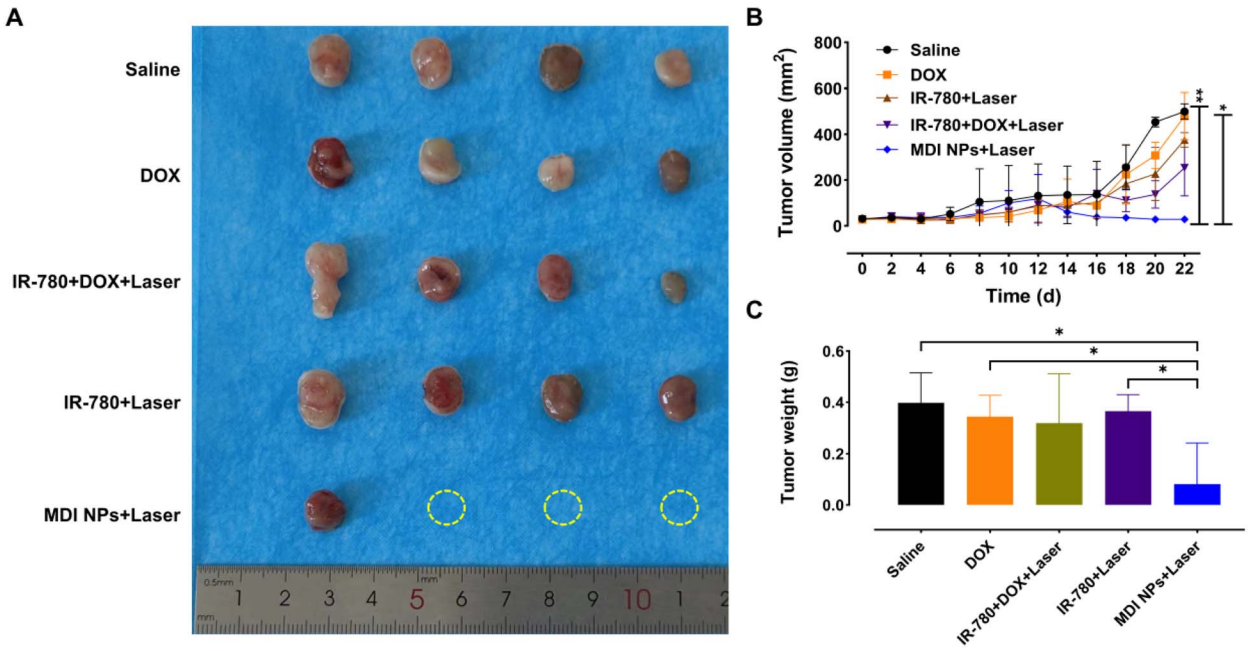

Fig. 7 *In vivo* antitumor efficacy of MDI NPs: (A) representative tumor images from different treatment groups; (B) tumor growth curves showing volume changes over time; (C) final tumor weights measured post-treatment. The yellow dashed circles represent the tumors that were cured after intervention. Error bars represent mean ± SD. *p < 0.05, **p < 0.01, ***p < 0.001, ****p < 0.0001.

significantly facilitated their prolonged circulation *in vivo* and effective accumulation at tumor sites.[38] The moderately negative surface charge characteristic effectively extended their blood circulation time.[39] Previous literature has confirmed that the acidic tumor microenvironment can trigger the degradation of PDA, thereby endowing it with pH-responsive release properties.[40] After being injected into the bloodstream *via* the tail vein, MDI NPs first preferentially accumulate in tumor tissues through the EPR effect. Subsequently, the surface PDA layer degrades first in the acidic environment, followed by the local release of IR-780 and DOX (which are hybrid-assembled in the PDA layer through π–π stacking interactions), with concomitant exposure of the Mn_3O_4 NPs core. This spatiotemporally controlled release mechanism enables a synergistic effect between photothermal therapy (mediated by IR-780 under laser irradiation) and chemotherapy (*via* DOX), maximizing therapeutic efficacy while minimizing off-target effects. The *in vitro* release experiments of MDI NPs confirmed the above hypothesis. Under simulated physiological conditions (pH 7.4), the cumulative release rates of DOX and IR-780 within 24 h were 19.9% and 9.9%, respectively, increasing only marginally to 22.4% and 11.3% after 72 h. This indicates that the PDA shell of MDI NPs forms an effective barrier, preventing premature drug leakage and ensuring the stability of the nanodelivery system during blood circulation. In contrast, under simulated tumor microenvironment conditions (pH 5.5), the degradation of the PDA shell in MDI NPs led to rapid drug release: within 24 h, the release of DOX reached 97.9%, while that of IR-780 was 71.7%. After 72 h, DOX release was nearly complete (99.5%), whereas IR-780 exhibited a lower total release (72.3%) due to its hydrophobicity. These results fully demonstrate the excellent pH-responsive drug release capability of MDI NPs, enabling tumor microenvironment-specific drug release and providing a critical foundation for *in vivo* targeted combination therapy. *In vivo* distribution results demonstrated that the fluorescence intensity of MDI NPs at tumor sites reached its peak at 24 hours post-injection and could be maintained for over 72 hours. In contrast, Wang *et al.* reported that free DOX reached maximum accumulation in major organs including liver, spleen, lungs and kidneys within 0.5 hours after tail vein injection, followed by rapid clearance within 24 hours.[41] These results clearly indicate that MDI NPs achieved sustained and targeted drug release to tumor tissues, enabling co-accumulation and synergistic action of both therapeutic molecules in tumor regions for over 72 hours. This approach not only enhanced therapeutic efficacy but also reduced dosing frequency and dosage, thereby minimizing drug side effects and potential drug resistance.

The *in vivo* MRI evaluation results were consistent with fluorescence imaging findings, demonstrating peak T_1-weighted contrast enhancement in tumors at 24 hours post-injection with clear visualization of tumor margins and internal architecture, followed by gradual signal attenuation (>72 hours). These results highlight the remarkable MRI diagnostic capability of MDI NPs, establishing a solid foundation for their theranostic applications. Acute toxicity tests confirmed excellent biocompatibility of MDI NPs, as the highest tested dose (135 mg kg^{-1}) caused no abnormalities in blood biochemical parameters, pathological changes in major organs, or mortality in mice. These findings collectively demonstrate the outstanding *in vivo* biocompatibility of MDI NPs.

Manganese-based contrast agents demonstrate remarkable advantages in MR imaging due to their unique physicochemical properties. Compared to conventional gadolinium- and iron-based counterparts, manganese-based agents exhibit superior characteristics including higher spin magnetization, faster water exchange rates, and enhanced biocompatibility, positioning them as promising alternatives.[42] The MDI NPs developed in this study achieved a remarkable r_1 relaxivity of 1.827 mM^{-1} s^{-1}, representing a 10.02-fold enhancement over bare Mn_3O_4 NPs (r_1 = 0.1824 mM^{-1} s^{-1}), which can significantly shorten the T_1 value of tissues, thereby enhancing the signal contrast between contrast agent-containing tissues and surrounding tissues on T_1-weighted images. This significant improvement primarily stems from the PDA coating facilitating efficient water access to paramagnetic manganese ions,[43] confirming MDI NPs' potential for T_1-weighted MRI and fulfilling the therapeutic monitoring capability envisioned in nanocarrier design. Regarding photothermal performance, MDI NPs demonstrated exceptional heating capacity, reaching 70–80 °C in aqueous solutions with consistent performance across different media, with a PCE of 47.6%. The nanoparticles maintained outstanding photothermal stability and tissue penetration capacity, with final temperatures remaining therapeutically effective despite moderate attenuation through muscle and fat layers. Notably, adipose tissue exhibited minimal impact on photothermal conversion capability, making MDI NPs particularly suitable for LPS treatment. *In vivo* studies verified that MDI NPs could effectively elevate local temperature to therapeutic levels, outperforming other IR-780-loaded nanocarriers in heating efficacy. These collective properties underscore the dual diagnostic and therapeutic potential of MDI NPs.[44,45]

Building upon these advantages, MDI NPs demonstrated outstanding synergistic antitumor effects both *in vitro* and *in vivo*. At the cellular level, comprehensive evaluations through cytotoxicity assays, colony formation tests, and live/dead cell staining consistently revealed that the combined MDI NPs + laser intervention significantly outperformed all monotherapy groups (DOX, IR-780) and the DOX + IR-780 + laser combination group. Quantitative analysis showed an exceptionally low CI of 0.17 for MDI NPs + Laser, representing marked improvement over the DOX-loaded IR-780 dye-labeled tube-forming peptoids (PepIR) nanotubes (CI = 0.323) developed by CAI *et al.*.[46] *In vivo* antitumor studies under mild photothermal conditions (808 nm laser, 3 min irradiation, 1 W cm^{-2} power, 43–45 °C) demonstrated that MDI NPs achieved superior tumor growth inhibition (94.3%) and a complete remission rate (75%), with significantly reduced tumor volume and weight compared to other treatment groups. These results compare favorably with the 94.4% inhibition rate reported by Deng *et al.* using upper critical solution temperature (UCST) thermosensitive nanomicelles NPUCST/(IR-780 + DOX) at 50 °C,[47] while avoiding the tissue damage risks associated with conventional high-temperature PTT (>50 °C).[48,49] Furthermore, under equivalent

thermal conditions, MDI NPs exhibited substantially enhanced therapeutic outcomes compared to existing therapies. The near-infrared-II emitting oligonucleotide-modified π-conjugated polymers (OCPNs) developed by Fan *et al.* achieved only 80% tumor suppression through combined PTT and gene therapy without complete remission,[50] while the hydrogen peroxide-responsive NIR-II AIE nanobombs PBPTV@mPEG(CO) reported by Ma *et al.* showed merely 40% cure rates,[51] highlighting the superior performance of MDI NPs. Furthermore, our results demonstrate that although all treatment regimens exhibit comparable efficacy against small tumors (≤100 mm^3), only the MDI NPs + laser combination achieves complete regression of larger tumors (>100 mm^3), while other treatment groups show continuous growth. This finding indicates that MDI NPs + laser therapy can maintain potent antitumor activity even as tumors progress to a larger volume, thereby providing a potential therapeutic strategy for the clinical treatment of locally advanced or drug-resistant tumors.

The multifunctional manganese-based nanotherapeutic system (MDI NPs) constructed in this study integrates chemotherapy, photothermal therapy, and MRI guidance, achieving a 94.3% tumor inhibition rate in LPS models and demonstrating significant theranostic potential. However, several challenges remain for its clinical translation: firstly, the precise regulation of multicomponent ratios and coating thickness during scalable production is difficult to standardize in large-scale manufacturing. Secondly, although the MRI capability of Mn_3O_4 NPs enables potential real-time monitoring, the long-term biosafety of manganese accumulation in non-target organs requires further verification through comprehensive chronic toxicity studies. Thirdly, despite the favorable photothermal conversion ability of MDI NPs, their absorption spectrum is mainly confined to the NIR-I region (650–900 nm). In contrast, photothermal agents responsive to the NIR-II region (1000–1700 nm) typically exhibit deeper tissue penetration and higher maximum permissible exposure doses.[52,53] Thus, future efforts may involve combining MDI NPs with NIR-II responsive materials to enhance therapeutic efficacy against deep-seated tumors. Additionally, manganese-based nanomaterials can activate the host immune system by increasing intracellular ROS levels or directly activating the cGAS-STING pathway.[54,55] Therefore, combining them with immunotherapy, photodynamic therapy (PDT), or chemodynamic therapy (CDT) to enhance efficacy,[56,57] along with further clarification of the underlying molecular mechanisms, is warranted.

5 Conclusion

This study successfully developed multifunctional manganese-based nanotheranostics (MDI NPs) by integrating Mn_3O_4 NPs, DOX and photosensitizer IR-780 with PDA surface modification, establishing a novel nanoplatform combining MRI capability with synergistic photothermal-chemotherapy. The MDI NPs demonstrated excellent stability, high relaxivity (r_1 = 1.827 mM^{-1} s^{-1}), excellent pH-responsive drug release capability and outstanding photothermal conversion efficiency (47.6%). Cellular studies revealed remarkable synergistic antitumor effects (CI = 0.17), while *in vivo* evaluation showed prolonged circulation and sustained drug release (>72 h) and favorable *in vivo* MRI imaging performance, with a 94.3% tumor suppression rate. The system provides a safe and effective novel strategy for LPS treatment with real-time therapeutic monitoring capability, representing a significant advancement in nanomaterial-based combination therapy for sarcomas. Future studies will focus on optimizing nanocomposites preparation for enhanced reproducibility and scalability, conducting comprehensive preclinical evaluations including long-term biodistribution, chronic toxicity, and photothermal conversion efficiency, and elucidating mechanistic synergies. These investigations will facilitate clinical translation, clarify the therapeutic mechanism of this multifunctional nanoplatform, and ultimately benefit LPS patients.

Author contributions

Wenhua Zhan: conceptualization, methodology, project administration, writing, review and editing. Shangting Du: methodology, data collection, analysis, writing, review and editing. Tianyi Zhu: data collection, analysis, writing. Yingying Liu: data collection, analysis. Lingyu Li: analysis. Yueyang Gao: data collection. Yijun Lu: data collection. Wei Wang: project administration, review and editing, final approval of completed version. All authors contributed to the article and approved the submitted version.

Conflicts of interest

There are no conflicts to declare.

Data availability

The data supporting this article have been included as part of the supplementary information (SI). Supplementary information is available. See DOI: **https://doi.org/10.1039/d5ra03568f**.

Acknowledgements

This work was supported, in part, by the Key Research and Development Program in Ningxia Province of China (No. 2023BEG03035), the Natural Science Basic Research Key Program of Ningxia Province of China (No. 2024AAC02079), the State Key Laboratory of Pathogenesis, Prevention and Treatment of High Incidence Diseases in Central Asia Fund (SKL-HIDCA-2024-NX1), and the Beijing Dadi Medical Charity Foundation (DDYL-A-KT-20250107-0003). The Health Re-search Program on Ningxia (2025-NWQP-B002). And some elements in the table of contents entry and Scheme 1 were obtained from **https://gdp.renlab.cn**.[58]

References

1 R. L. Siegel, A. N. Giaquinto and A. Jemal, *Ca-Cancer J. Clin.*, 2024, **74**, 12–49.

2 J. M. Brownstein and T. F. DeLaney, *Hematol./Oncol. Clin. North Am.*, 2020, **34**, 161.
3 J. H. Choi and J. Y. Ro, *Adv. Anat. Pathol.*, 2021, **28**, 44–58.
4 M. S. Anju, C. Chandramohan, R. V. Bhargavan, T. Somanathan and L. Subhadradevi, *J. Mol. Histol.*, 2024, **55**, 227–240.
5 S. Bonvalot, A. Gronchi, P. Hohenberger, S. Litiere, R. E. Pollock, C. P. Raut, P. Rutkowski, D. Strauss, C. J. Swallow and F. Van Coevorden, *Ann. Surg Oncol.*, 2015, **22**, 256–263.
6 S. Singer, C. R. Antonescu, E. Riedel and M. F. Brennan, *Ann. Surg.*, 2003, **238**, 358–370.
7 I. Judson, J. Verweij, H. Gelderblom, J. T. Hartmann, P. Schöffski, J. Y. Blay, J. M. Kerst, J. Sufliarsky, J. Whelan, P. Hohenberger, A. Krarup-Hansen, T. Alcindor, S. Marreaud, S. Litière, C. Hermans, C. Fisher, P. C. W. Hogendoorn, A. P. dei Tos, W. T. A. van der Graaf, O. European and S. Treatment, Canc Soft Tissue Bone, *Lancet Oncol.*, 2014, **15**, 415–423.
8 M. Sheibani, Y. Azizi, M. Shayan, S. Nezamoleslami, F. Eslami, M. H. Farjoo and A. R. Dehpour, *Cardiovasc. Toxicol.*, 2022, **22**, 292–310.
9 C. L. Haddox, J. L. Hornick, C. L. Roland, E. H. Baldini, V. L. Keedy and R. F. Riedel, *Cancer Treat Rev.*, 2024, **131**, 102846.
10 T. Assi, C. Ngo, M. Faron, B. Verret, A. Lévy, C. Honoré, C. Hénon, C. Le Péchoux, R. Bahleda and A. Le Cesne, *Curr. Treat. Options Oncol.*, 2023, **24**, 1598–1613.
11 H. Maeda, J. Wu, T. Sawa, Y. Matsumura and K. Hori, *J. Contr. Release.*, 2000, **65**, 271–284.
12 R. K. Jain and T. Stylianopoulos, *Nat. Rev. Clin. Oncol.*, 2010, **7**, 653–664.
13 M. Overchuk, R. A. Weersink, B. C. Wilson and G. Zheng, *ACS Nano*, 2023, **17**, 7979–8003.
14 H. Wang, Y. Chen, R. Wei, J. L. Zhang, J. H. Zhu, W. B. Wang, Z. F. Wang, Z. Wupur, Y. J. Li and H. Meng, *Adv. Mater.*, 2024, **36**, e2309591.
15 L. Li, X. Q. Liang, T. He, X. C. Li, X. Z. Huang, N. Wang, M. L. Shen, Y. Q. Shu, R. Wu, M. M. Zhang, Q. J. Wu and C. Y. Gong, *Biomaterials*, 2022, 290.
16 X. S. Li, J. F. Lovell, J. Yoon and X. Y. Chen, *Nat. Rev. Clin. Oncol.*, 2020, **17**, 657–674.
17 X. D. Zeng, Y. L. Xiao, J. C. Lin, S. S. Li, H. Zhou, J. X. Nong, G. Z. Xu, H. B. Wang, F. C. Xu, J. Z. Wu, Z. X. Deng and X. C. Hong, *Adv. Healthc. Mater.*, 2018, **7**, e1800589.
18 S. F. Duan, Y. L. Hu, Y. Zhao, K. Y. Tang, Z. J. Zhang, Z. L. Liu, Y. Wang, H. Y. Guo, Y. C. Miao, H. D. Du, D. L. Yang, S. K. Li and J. J. Zhang, *RSC Adv.*, 2023, **13**, 14443–14460.
19 G. M. Hahn and E. C. Shiu, *Cancer Res.*, 1983, **43**, 5789–5791.
20 C. Xu and K. Y. Pu, *Chem. Soc. Rev.*, 2021, **50**, 1111–1137.
21 A. P. Dei Tos, *Ann. Diagn. Pathol.*, 2000, **4**, 252–266.
22 S. G. Balwe, D. Moon, M. Hong and J. M. Song, *Nano Convergence*, 2024, **11**, 48.
23 X. Y. Xu, J. L. Duan, Y. Liu, Y. Kuang, J. L. Duan, T. Liao, Z. Q. Xu, B. B. Jiang and C. Li, *Acta Biomater.*, 2021, **126**, 445–462.
24 Z. B. Yue, X. Y. Wang, T. Yu, S. J. Shang, G. Y. Liu, W. W. Jing, H. Z. Yang, Y. H. Luo and X. R. Jiang, *Magn. Reson. Imaging*, 2022, **91**, 91–99.
25 H. Lee, S. M. Dellatore, W. M. Miller and P. B. Messersmith, *Science*, 2007, **318**, 426–430.
26 Y. Liu, K. Ai and L. Lu, *Chem. Rev.*, 2014, **114**, 5057–5115.
27 Z. Wang, Y. Duan and Y. Duan, *J. Contr. Release*, 2018, **290**, 56–74.
28 A. Jin, Y. Wang, K. Lin and L. Jiang, *Bioact. Mater.*, 2020, **5**, 522–541.
29 B. Yu, J. Liu, S. Liu and F. Zhou, *Chem Commun.*, 2010, **46**, 5900–5902.
30 J. W. Wojtkowiak, D. Verduzco, K. J. Schramm and R. J. Gillies, *Mol. Pharm.*, 2011, **8**, 2032–2038.
31 W. Zheng, H. Fan, L. Wang and Z. Jin, *Langmuir*, 2015, **31**, 11671–11677.
32 Z. Yang, C. Wang, S. Du, Q. Ma, W. Wang, C. liu, Y. Zhan and W. Zhan, *Biomed. Eng. Online*, 2024, **23**, 53.
33 S. He, Q. Zheng, L. Ma, H. Shen, B. Zheng, Y. Zhang, H. H. Deng, W. Chen and K. Fan, *Nano Lett.*, 2024, **24**, 14337–14345.
34 T. C. Chou, *Cancer Res.*, 2010, **70**, 440–446.
35 W. J. Xu, X. Qing, S. L. Liu, D. L. Yang, X. C. Dong and Y. W. Zhang, *Small*, 2022, 18.
36 S. Y. Wang, Y. Cui, T. Dalani, K. Y. Sit, X. L. Zhuo and C. K. Choi, *Chem. Commun.*, 2024, **60**, 2982–2993.
37 X. N. An, A. J. Zhu, H. H. Luo, H. T. Ke, H. B. Chen and Y. L. Zhao, *ACS Nano*, 2016, **10**, 5947–5958.
38 A. Z. Wang, R. Langer and O. C. Farokhzad, in *Annual Review Of Medicine*, ed. C. T. Caskey, C. P. Austin and J. A. Hoxie, 2012, vol. 63, pp. 185–198.
39 F. Alexis, E. Pridgen, L. K. Molnar and O. C. Farokhzad, *Mol. Pharm.*, 2008, **5**, 505–515.
40 Y. L. Liu, K. L. Ai and L. H. Lu, *Chem. Rev.*, 2014, **114**, 5057–5115.
41 Y. Wang, Y. S. Wu, K. Li, S. H. Shen, Z. Y. Liu and D. C. Wu, *Adv. Funct. Mater.*, 2019, **29**, 1805582.
42 R. C. Du, Z. W. Zhao, J. Cui and Y. A. Li, *Int. J. Nanomed.*, 2023, **18**, 6077–6099.
43 X. Ding, J. H. Liu, J. Q. Li, F. Wang, Y. H. Wang, S. Y. Song and H. J. Zhang, *Chem. Sci.*, 2016, **7**, 6695–6700.
44 Y.-J. Lu, A. T S, C.-C. Chuang and J.-P. Chen, *Cancers*, 2021, **13**, 3690.
45 H. T. Huang, J. Fu, H. L. Y. Peng, Y. Y. He, A. Q. Chang, H. Z. Zhang, Y. Hao, X. H. Xu, S. M. Li, J. X. Zhao, J. Ni and X. X. Dong, *J. Nanobiotechnol.*, 2024, **22**, 647.
46 X. L. Cai, M. M. Wang, P. Mu, T. Y. Jian, D. Liu, S. C. Ding, Y. A. Luo, D. Du, Y. Song, C. L. Chen and Y. H. Lin, *Research*, 2021, 2021.
47 Y. Y. Deng, F. Käfer, T. T. Chen, Q. Jin, J. Ji and S. Agarwal, *Small*, 2018, 14.
48 Y. Zou, M. L. Li, T. Xiong, X. Z. Zhao, J. J. Du, J. L. Fan and X. J. Peng, *Small*, 2020, 16.
49 M. Rybinski, Z. Szymanska, S. Lasota and A. Gambin, *J. R. Soc. Interface*, 2013, **10**, 20130527.

50 G. L. Fan, S. X. Hou, Y. Gu, H. F. Jiang, W. K. Zhang, W. T. Wu, M. Y. Wang and L. L. Tian, *Angew. Chem., Int. Ed.*, 2025, **64**, e202425654.
51 G. C. Ma, Z. K. Liu, C. G. Zhu, H. J. Chen, R. T. K. Kwok, P. F. Zhang, B. Z. Tang, L. T. Cai and P. Gong, *Angew. Chem., Int. Ed.*, 2022, **61**, e202207213.
52 J. Liu, L. Liang, P. Gan, F. Lin, Z. Dai, Z. Chen, Y. Xu, Q. Yang, M. Cao, S. Wang, Y. Gu, Z. Yuan, Q. Zhong, D. Hu and Y. Yao, *J. Med. Chem.*, 2025, **68**, 7592–7604.
53 L. Feng, C. Li, L. Liu, Z. Wang, Z. Chen, J. Yu, W. Ji, G. Jiang, P. Zhang, J. Wang and B. Z. Tang, *ACS Nano*, 2022, **16**, 4162–4174.
54 M. Lv, M. Chen, R. Zhang, W. Zhang, C. Wang, Y. Zhang, X. Wei, Y. Guan, J. Liu, K. Feng, M. Jing, X. Wang, Y. C. Liu, Q. Mei, W. Han and Z. Jiang, *Cell Res.*, 2020, **30**, 966–979.
55 J. Chandra, S. M. Teoh, P. Kuo, L. Tolley, A. A. Bashaw, Z. K. Tuong, Y. Liu, Z. Chen, J. W. Wells, C. Yu, I. H. Frazer and M. Yu, *J. Immunol.*, 2021, **206**, 987–998.
56 J. Ma, N. Li, J. Wang, Z. Liu, Y. Han and Y. Zeng, *Exploration*, 2023, **3**, 20220161.
57 P. Yang, J. Zhang, Y. Chang, L. Tang, G. Ma, X. Liu, F. Gao, X. Ma and Y. Guo, *J. Inorg. Biochem.*, 2025, **272**, 113005.
58 S. Jiang, H. Li, L. Zhang, W. Mu, Y. Zhang, T. Chen, J. Wu, H. Tang, S. Zheng, Y. Liu, Y. Wu, X. Luo, Y. Xie and J. Ren, *Nucleic Acids Res.*, 2025, **53**, D1670–d1676.